Research Article | Vol. 14, No. 10 / 1 Oct 2023 / Biomedical Optics Express 5338

Biomedical Optics EXPRESS

Development and evaluation of a wearable peripheral vascular compensation sensor in a swine model of hemorrhage

FRANCESCA BONETTA-MISTELI,[1] TOI COLLINS,[2] TODD PAVEK,[2] MADISON CARLGREN,[1,3] DEREK BASHE,[1,4] ANTONINA FROLOVA,[3] LEONID SHMUYLOVICH,[4,5] AND CHRISTINE M. O'BRIEN[1,3,*]

[1] *Department of Biomedical Engineering, Washington University in St. Louis; St. Louis, USA*
[2] *Division of Comparative Medicine, Washington University in St. Louis; St. Louis, USA*
[3] *Department of Obstetrics & Gynecology, Washington University in St. Louis; St. Louis, USA*
[4] *Department of Radiology, Washington University in St. Louis; St. Louis, USA*
[5] *Department of Dermatology, Washington University in St. Louis; St. Louis, USA*
[*] *c.obrien@wustl.edu*

Abstract: Postpartum hemorrhage (PPH) is the leading and most preventable cause of maternal mortality, particularly in low-resource settings. PPH is currently diagnosed through visual estimation of blood loss or monitoring of vital signs. Visual assessment routinely underestimates blood loss beyond the point of pharmaceutical intervention. Quantitative monitoring of hemorrhage-induced compensatory processes, such as the constriction of peripheral vessels, may provide an early alert for PPH. To this end, we developed a low-cost, wearable optical device that continuously monitors peripheral perfusion via laser speckle flow index (LSFI) to detect hemorrhage-induced peripheral vasoconstriction. The measured LSFI signal produced a linear response in phantom models and a strong correlation coefficient with blood loss averaged across subjects (>0.9) in a large animal model, with superior performance to vital sign metrics.

© 2023 Optica Publishing Group under the terms of the Optica Open Access Publishing Agreement

1. Introduction

Postpartum hemorrhage (PPH) is the leading cause of maternal mortality globally, accounting for 27% of maternal deaths worldwide [1]. Fortunately, early diagnosis and treatment significantly reduces mortality and morbidity associated with PPH [2–7]. The principal cause of PPH is uterine atony, in which the uterus fails to contract and close the vessels at the placental attachment site that previously perfused the placenta at a rate of 600-700 mL blood/min [8,9]. Treatment in the early stages of hemorrhage includes low-cost and accessible options such as pharmacologic agents and intrauterine devices that can stop blood loss [10]. Later stages of hemorrhage require blood transfusion and surgical interventions because the significant blood volume lost must be replenished and blood loss must be immediately halted. Unfortunately, these treatments are often not accessible depending upon where a patient lives [11,12], underscoring the importance of early diagnosis and treatment.

While early detection of PPH is critical, it is also challenging because of physiologic compensation mechanisms that can mask excessive bleeding. In early hemorrhage, the sympathetic nervous system becomes activated to ensure adequate perfusion of vital organs, and in turn, vital signs remain stable [13,14]. In many patients, particularly young patients of childbearing age, blood pressure is maintained by increases in systemic vascular resistance (SVR) caused by peripheral vasoconstriction. This mechanism offsets decreases in cardiac output (CO) caused by blood loss, and thus decreases in blood pressure are delayed until compensatory responses are depleted. Some patients may have a blunted compensatory response in which increases in SVR do not fully offset decreases in CO, and consequently mean arterial pressure (MAP) gradually

#494720 https://doi.org/10.1364/BOE.494720
Journal © 2023 Received 5 May 2023; revised 13 Aug 2023; accepted 17 Aug 2023; published 21 Sep 2023

Biomedical Optics EXPRESS

drops. The American College of Obstetricians and Gynecologists define PPH as the cumulative loss of 1000 mL of blood or signs or symptoms of hypovolemia (low levels of extracellular body fluids) within 24 hours of delivery [15]. Worldwide, the most common method for PPH diagnosis is visual estimation of blood loss (mL) due to its simplicity and zero added cost. However, it has been shown to underestimate blood loss up to 75%, with the magnitude of error increasing with increased PPH severity [16,17]. Several tools have been developed to help quantify blood loss [18,19], but many are labor-intensive and cannot detect occult (hidden) blood loss which is common in uterine atony. In addition to estimation of blood loss, providers may rely on vital signs such as heart rate (HR), respiratory rate, peripheral blood oxygenation (SpO_2), and blood pressure [20,21]. However, because of stabilization due to the compensatory responses discussed above, they are most effective in settings of massive PPH (>1500 mL blood loss) when compensatory responses are exhausted and blood replacement products and surgical intervention are required [20,21]. As such, there is an unmet need for a continuous monitoring method for *early* signs of PPH that is inexpensive, accessible, and sensitive to both external and internal bleeding.

Healthcare teams do not currently have tools that monitor peripheral compensation responses which could provide an early indication of hemorrhage. We hypothesized that a wrist-worn light-based perfusion measurement, the laser speckle flow index (LSFI), could address this clinical need [13,22–24]. Blood flow magnitude is inversely proportionate to resistance [25], and thus continuous measurement of peripheral blood flow by LSFI could detect the body's compensation to hemorrhage. LSFI uses a laser and a camera to detect and quantify spatial and temporal changes in speckle patterns to extract flow information and is linearly proportional to blood flow [26–28]. Wearable laser speckle imaging sensors have been developed to provide real-time monitoring of perfusion and cardiovascular physiology [29,30]. However, to our knowledge there are no current laser speckle imaging wearables that are wireless, wrist-worn, or developed for use monitoring vasoconstriction in response to blood loss. Furthermore, LSFI has a high signal-to-noise ratio (SNR) and is minimally affected by skin color [31], providing excellent signal quality [29]. We have developed a custom wrist-worn wearable LSFI sensor to detect early hemorrhage-associated changes in peripheral perfusion. The device is small, simple, battery-powered, and transmits data wirelessly via Bluetooth to track results from a mobile device such as a tablet. Such characteristics are ideal for patient monitoring, as evidenced by the pulse oximeter, a light-based device used globally for patient monitoring. Herein, we characterized the sensor's optical performance, validated a linear response from flow phantoms across a range of flow rates, and demonstrated utility as an early detection tool for hemorrhage in a swine model of fixed-volume hemorrhage, in which known volumes of blood, based on the estimated blood volume of the swine, are removed over a period of time [32].

2. Materials and methods

2.1. Study design

This study was designed to test whether a custom wearable perfusion sensor could detect peripheral vasoconstriction caused by hemorrhage, reflecting a well-studied sympathetic nervous system compensatory response to hypovolemia [22–24], that could offer early detection of hemorrhage. A swine fixed-volume hemorrhage model was used to test the device performance because their cardiovascular physiology closely resembles human physiology [32]. The performance of the device was quantified by the strength of the relationship between measured LSFI and net fluid volume changes in the swine subject during periods of facilitated blood loss and fluid infusion. A sample size of five swine was used for this study. The hemorrhage procedure included a baseline recording, repeated blood draws, followed by resuscitation via intravenous fluids. The procedure was not randomized or blinded to the study team.

Biomedical Optics EXPRESS

2.2. Sensor hardware design

Laser speckle contrast imaging utilizes a laser and camera to measure relative blood flow through changes in the laser speckle pattern produced when laser light interacts with tissue. Laser speckle systems can be configured in either transmission or reflection modes. The wearable laser speckle-based peripheral perfusion sensor was configured in reflectance mode, with the excitation source consisting of a 50 mW 785 nm laser diode (Laserland, 11071013). The laser had an elliptical spot size with full-width at half maximum dimensions of 3.8 mm and 2.2 mm, resulting in a spot size of 0.26 cm^2, and which had an irradiance (0.19 W/cm^2) below ANSI's maximum permissible exposure limits (0.3 W/cm^2) for skin [33]. This wavelength was chosen because near infrared sources have higher tissue penetration depth and minimum melanin absorption [34], thus reducing skin pigmentation-based signal bias while still operating at a wavelength that is sensitively detected by inexpensive silicon-based CMOS detectors. The center-to-center distance between the CMOS sensor and laser was set to 11 mm, enabling collection of diffusely scattered photons that have interacted with subsurface blood vessels [30]. The sensor system consists of a double-lens Raspberry Pi camera Module v2 NoIR. This camera has an 8MP Sony IMX219 CMOS sensor and no infrared (IR) filter, allowing the camera to detect IR light. The camera is capable of acquiring 3280×2464 pixel images and recording video at 1080p@30 frames per second (fps). For this study, recording at 320×240p allowed 100 fps, and 80 fps was possible at 640×480p. The sensor size is 3.68×2.76 mm, with each pixel being 1.12×1.12 µm. Although the physical pixel size is a characteristic of the sensor, when the resolution is reduced to 640×480 or 320×240 under default settings, the camera sensor performs 2×2 or 4×4 pixel binning, increasing the pixel size by a factor of 2 or 4, respectively.

A double-lens system was constructed by mounting the original Raspberry Pi camera fixed focus lens [35] on the module and introducing a second identical lens in an inverted position placed at the surface of the first lens. A 0.4 mm thick, 7.5 mm diameter sapphire optical window (Edmond Optics, 43-628) was placed on the surface of the second lens, allowing the system to be in focus when an object is in direct contact with the window. This configuration enabled microscopic resolution from a short optical train [36] of 6.42 mm. Such miniaturization is ideal for wearable devices which require a small footprint.

The device is controlled by a Raspberry Pi Zero 2W computer and powered by either wall power or a PiSugar 1200 mAh battery (Guangzhou Soft Electric Technology Co., Ltd., Guangzhou, China). The Pi Sugar battery is an uninterruptible power source that can supply power and charge simultaneously, allowing the device to be wireless while maintaining voltage regulation. A custom PCB provided a stable 3.3 V to the laser diode from a constant 5 V pin on the Raspberry Pi computer and a general-purpose input/output (GPIO) pin was used for laser control.

2.3. Sensor software design

The device software, written in Python, controlled the laser diode and camera functionality. The Raspberry Pi computer interfaced with a PC laptop via Bluetooth connection (Fig. 1). In this connection, the Raspberry Pi was the server and the PC was the client. The PC took user input to turn on/off the laser diode and record laser speckle videos for a specified length of time. The Raspberry Pi carried out desired tasks, saved recorded speckle videos, processed video data, and sent processed data to the PC. The PC received, saved, and plotted data as a function of time. This program allowed for near real-time (15-20 second delay after data acquisition) data visualization for monitoring blood flow.

To extract LSFI, laser speckle contrast (K) was first computed on the Raspberry Pi Zero 2W computer using a custom algorithm for fast processing. Each frame from the video was processed using the spatial processing algorithm to calculate the laser speckle contrast image [28]. A 7×7 sliding window translated across a raw intensity image to produce a speckle contrast value (K)

Biomedical Optics EXPRESS

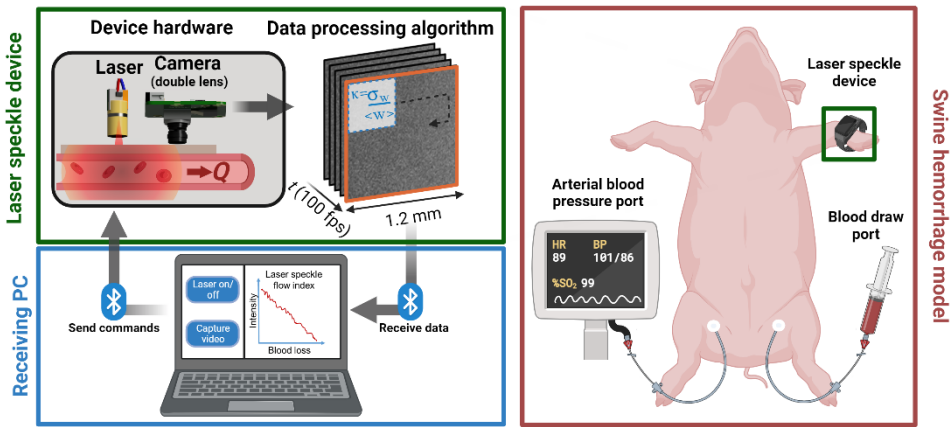

Fig. 1. Data acquisition and visualization via Bluetooth communication used in swine studies. Left) User inputs to control laser and video capture are sent to the Raspberry Pi. Images are recorded and processed on the device and sent back to the computer where they are automatically plotted. Right) Experimental setup for swine hemorrhage model, with blood draw port and arterial blood pressure port. Device was worn on the swine's "wrist".

for each window within the frame:

$$K = \frac{\sigma(I)}{\langle I \rangle} \tag{1}$$

where $\sigma(I)$ is the standard deviation of pixel intensity within the window and $\langle I \rangle$ is the mean pixel intensity within the window. Following the mathematical process outlined by Tom et. al. [37], Eq. (1) can bes rewritten in terms of summations of pixel intensities and squared pixel intensities:

$$K = \frac{\sqrt{\frac{n^2 \sum_{i=1}^{n^2} I_i^2 - \left(\sum_{i=1}^{n^2} I_i\right)^2}{n^2(n^2-1)}}}{\frac{\sum_{i=1}^{n^2} I_i}{n^2}}, \tag{2}$$

where n x n is the dimensions of the sliding window. This is equivalent to convolving the raw image and square of the raw image with an nxn matrix of ones. We found that computation speed can increase while retaining the speckle contrast value by convolving with an nxn identity matrix:

$$K = \frac{\sqrt{\frac{nI_s^2 \otimes \begin{pmatrix} 1 & \cdots & 0 \\ \vdots & 1 & \vdots \\ 0 & \cdots & 1 \end{pmatrix} - \left(I_s \otimes \begin{pmatrix} 1 & \cdots & 0 \\ \vdots & 1 & \vdots \\ 0 & \cdots & 1 \end{pmatrix} \right)^2}{n(n-1)}}}{\frac{I_s \otimes \begin{pmatrix} 1 & \cdots & 0 \\ \vdots & 1 & \vdots \\ 0 & \cdots & 1 \end{pmatrix}}{n}}, \tag{3}$$

where I_s is the raw image and I_s^2 is the square of the raw image. An efficient computational approach to calculate these convolutions is to generate 'diagonal speckle sums' I_{ds} and I_{ds}^2 for

Biomedical Optics EXPRESS

both the raw image and the square of the image, respectively:

$$I_{ds} = I_s + I_{s:x+1,y+1} + \ldots + I_{s:x+n-1,\, y+n-1}, \tag{4}$$

$$I_{ds}^2 = I_s^2 + I_{s:x+1,\, y+1}^2 + \ldots + I_{s:x+n-1,\, y+n-1}^2, \tag{5}$$

where $I_{s:x+k,y+k}$ and $I^2_{s:x+k,\, y+k}$ are the raw image and square of the raw image offset k pixels along the diagonal. The diagonal speckle sums can then be used instead of the convolutions to generate a pixel-by-pixel speckle contrast value via the following equation:

$$K = \frac{\sqrt{\frac{nI_{ds}^2 - {I_{ds}}^2}{n(n-1)}}}{\frac{I_{ds}}{n}}, \tag{6}$$

The mean value of K across all imaging pixels defines K. The Raspberry Pi computer implemented the algorithm in Python and transmitted K to the receiving PC. K was then converted to the laser speckle flow index (LSFI), which is a measure proportionate to blood flow (perfusion), via the following equation:

$$LSFI = \frac{1}{2 * T * <K>^2}, \tag{7}$$

where T is the camera exposure time. This process was repeated for every frame of the laser speckle video, resulting in a time-varying pulsatile waveform known as the speckle-plethysmogram (SPG) [29]. A wide moving average filter applied to the waveform removed pulsatile variation and produced a clean mean LSFI signal.

2.4. Impact of camera system parameters on laser speckle

High-contrast laser speckle imaging requires proper spatial or temporal sampling. Spatial sampling provides higher temporal resolution to observe rapidly changing phenomena such as blood flow. Optimization of the imaging system allows for observation of the full laser speckle pattern. The minimum speckle size should be greater than two times the pixel size to surpass the Nyquist sampling rate. Speckle size can be calculated using the equation:

$$S = 2.44\lambda(1 + M)f/\#, \tag{8}$$

in which λ is the wavelength of the coherent light source, M is the magnification of the camera system, and $f/\#$ is the f number of the camera system [28].

Two recording modes were used during data acquisition for in vitro and in vivo experiments: 640×480p @ 80fps and 320×240p @ 100fps. Capturing 640×480 and 320×240 pixel videos at 80 and 100 fps, respectively, of a resolution test target (Thorlabs, R1DS1P) enabled the determination of the double-lens camera system magnification by comparing the physical pixel size to the object size per pixel:

$$M = \frac{physical\ pixel\ size}{object\ size\ per\ pixel}. \tag{9}$$

The object size per pixel was calculated for each recording using MATLAB. Physical pixel size was determined by considering pixel binning under each set of recording parameters.

The f/# of the system was found in the Raspberry Pi v2 camera module documentation, and experimentally verified using the equation:

$$f/\# = \frac{f}{D}, \tag{10}$$

where f represents the focal length of the system and D represents the diameter of the lens. The Raspberry Pi documentation provided the $f/\#$ and f of the single lens system which were used to

Biomedical Optics EXPRESS

solve Eq. (10) for the diameter of the lens which was verified by physical measurement of the lens aperture.

The spatial resolution of the system was found by plotting the pixel intensities of a row that spanned across a set of 3 lines on an USAF resolution test target (Thorlabs) and ensuring a step function was observed. This process was performed on multiple sets of lines until the smallest line thickness that produced a step function was determined.

2.5. Laser characterization

To ensure laser stability over time while in use, the spectral profile and power of the low-cost laser were recorded every 10 minutes over a six-hour period using a spectrometer (Flame Spectrometer, Ocean Optics) and an optical power meter (PM100D and S121C, Thorlabs). An identical experiment conducted for benchmarking performance used a high-cost laser system that included a pigtail laser (LP785-SAV50, Thorlabs), laser mount (LDM9LP), temperature controller (TED 200, Thorlabs), and current driver (LDC 205 C, Thorlabs), and cost ~100X more than the low-cost laser diode. The spectral profile and power of the low-cost laser at temperatures ranging from 8.8-38.4°C (8.8, 18.4, 27.4, 32.7, 35.4, 38.4 °C), representing the range of possible ambient temperatures a patient might experience, were also measured to provide the stability of the laser with varying temperatures. Changes in the peak wavelength and optical power output of the laser diode were evaluated as parameters of stability. Operating the lasers within a 0°C cold room lowered the temperature, while warm air from a heat gun (840015, Kawasaki) raised the temperature. An infrared camera (E6-XT, FLIR) monitored the temperature. In addition, mean LSFI was calculated from measurements over a 15 second period while recording a static piece of white paper (minimum) or a blood flow phantom (described in Section 2.7) at a 20 mm/s (maximum) to determine the distribution of pixel intensities and the range of speckle values produced using each laser. The LSFI was measured at 100 fps with an exposure time of 5 ms to mirror the parameters used in the swine hemorrhage model.

2.6. Device power consumption

The power consumption of each device during various states was measured using a digital multimeter (Eversame, 00005). Power consumption was monitored during idle states, data collection, and data transmission modes. Additionally, the electric charge (ampere-hours) consumed by the device over a 30-minute recording period was measured to determine the battery capacity required to power the device.

2.7. Device performance in vitro

In vitro testing of the laser speckle device was performed using an optical tissue-mimicking flow phantom across a range of physiologically relevant velocities [38,39]. When volume is lost during hemorrhage, the body responds by decreasing the diameter of vessels in the periphery, which increases resistance. Blood flow follows the path of least resistance, and thus shunts a higher proportion of blood to the core and a lower proportion to the periphery. This drop in peripheral flow also results in a decrease in blood velocity. Custom optical 3D printed flow phantoms (protocol described in Supplement) were created and contained a 1.6 mm diameter horizontal channel throughout the phantom. A syringe containing 2% intralipid fluid (l141, Sigma-Aldrich, St. Louis, MO) was connected to the hollow channel of the optical flow phantom using a luer lock needle. A syringe pump (Ne-1000, New Era Pump Systems Inc.) pushed fluid through the optical phantom at velocities ranging between 0 and 10 mm/s [38,39]. Fluid was pumped for 20 seconds at each velocity and laser speckle video was recorded for the last 3 seconds of each interval to allow the channel pressure to equilibrate at each velocity. Images were acquired at an exposure of 0.5 ms, a resolution of 640p, and 80 fps, resulting in laser speckle images that surpassed Nyquist criteria for speckle size. The higher resolution recording mode was used for

Biomedical Optics EXPRESS

high speckle quality and the 0.5 ms exposure time was chosen to optimize system sensitivity. The mean LSFI over the 3-second interval was calculated for each velocity.

2.8. Device performance in swine model of hemorrhage

All swine studies were performed under an approved IACUC protocol with supervision by veterinary staff at Washington University in St. Louis, Division of Comparative Medicine. To minimize inter-subject variability, the study used 11-week-old male Yorkshire and Landrace crossbreed pigs (Oak Hill Genetics, Ewing, IL). The average weight of the pigs was 37.09 kg and the range of weights was 33.57-43.18 kg.

All pigs had a standard laboratory diet with ad-lib access to water prior to beginning the experiments. Pigs were fasted from food for 12 hours prior to the start of the procedure. All hemorrhage studies were acute, with all pigs euthanized using intravenous (IV) potassium chloride immediately after the completion of hemorrhage and volume resuscitation procedures.

A telazol/ketamine/xylazine cocktail (TKX), given intramuscularly, sedated the swine, followed by intubation with a 6- or 7-mm endotracheal tube. Isoflurane gas maintained the surgical plane of anesthesia for the animals and prevented pain, distress, and movement during the experiments. Vital signs were monitored throughout the study using a thermometer to track temperature and multiple sensors that were connected to a Surgivet Advisor Tech Vital Signs Monitor (Smiths Medical, Plymouth, MN). These included a pulse oximeter applied to the swine tongue to measure SpO_2 and HR as well as invasive pressure catheters to track arterial blood pressure. An ear vein catheter provided the animals with IV fluids and intraoperative medications. For the first hour under anesthesia, swine received IV fluids at a drip rate of 6 ml/min, followed by a drip rate of 3 mL/min until the end of the procedure. Prior to initiation of the study, the animals were placed in a supine position on a heated operating table and maintained on positive pressure ventilation (7 cm H_2O) with a tidal volume of 10 ml/kg, a respiratory rate of 8-14/minute, and end-tidal CO_2 kept within 30-45 mmHg. Blood glucose was maintained >60 mg/dL via supplemental dextrose IV as needed. Swine 4 experienced several blood clots in the femoral catheter line, making blood collection difficult. The next pig (swine 5) was heparinized (150 IU/kg IV) to prevent blood clotting; however, effects on peripheral perfusion were noted (hypotension and non-reactive peripheral vessels in response to hemorrhage). Subsequent pigs were not heparinized. Instead, a heparinized saline (6 IU/ml) lock was maintained in the large bore pressure catheters.

In the first swine, placement of vascular access sheaths (7F) in the left femoral vein and right femoral artery was performed using surgical dissection. Subsequent vascular access sheaths were placed in the other pigs using either surgical dissection or an ultrasound-guided percutaneous technique. The left femoral vein sheath was used for blood removal to induce hemorrhagic shock, however, the vein collapsed during blood removal. In all subsequent swine, blood was withdrawn from the left femoral artery, as the artery is less likely to collapse during blood removal due to more muscular tone. The right femoral catheter measured systolic, diastolic, and MAP via the Surgivet Adivsor Monitor. Three study pigs also had a vascular access sheath (7F) placed in the right external jugular vein via surgical dissection. Catheters placed in the external jugular vein measured central venous pressure (CVP) and patency was maintained via heparinized saline as described above. Experienced laboratory animal veterinarians inserted all catheters.

Preparation for the placement of the laser speckle device included shaving the left posterior carpus of the swine, which minimized interference with the sensor, and affixing the sensor to the shaved area after sedation. A minimum 20-minute baseline recording occurred before initiating the hemorrhage protocol. The LSFI device recorded with a resolution of 320p and an exposure time of 5 ms at 100 fps for 10 seconds of each minute and calculated the mean over each 10-second interval. A frame rate of 100 fps and a resolution of 320p was chosen to maximize temporal resolution during data acquisition. A 5 ms exposure time was used as this is widely

Biomedical Optics EXPRESS

accepted as an optimal in vivo recording parameter [40]. A 5-frame moving average smoothed the data collected during the study.

The fixed-volume hemorrhage protocol was followed by removing either 1.5 or 3% estimated blood volume (EBV) every 2.5 or 5 minutes until either a total of 40% EBV had been removed, MAP neared 40, or the attending veterinarian concluded that the swine was in shock. Estimated blood volume was calculated using the following relationship: 58-74 ml/kg [32], and the average value of 66 ml/kg was used for EBV calculations. Once blood withdrawal ceased, no intervention was given for 10 minutes. After the 10-minute pause, IV infusion with crystalloids (NaCl saline solution or Lactated Ringers Solution) at 1.5-3% EBV occurred every 5 minutes for a total of 30 minutes. Throughout the procedure, blood was collected in heparinized 1 mL syringes and used to measure blood gas, hematocrit, sodium, chlorine, calcium, glucose, and lactose contents of the blood in 15-minute intervals. Vital signs including HR, core temperature, respiration rate, CVP, and blood oxygen saturation (SpO_2) were also monitored by veterinary staff and included in the study results.

2.9. Statistical analysis

A Pearson correlation was used to quantify the linear relationship between the measured physiologic parameters (LSFI, shock index (SI, ratio of HR and systolic blood pressure), MAP, HR) and EBV. A best-fit line was fit to each comparison and the slope of the line was reported. The average correlation coefficient and slope for each measurement type per swine were then calculated. In addition, a Pearson correlation was also performed on the pooled swine data. The analysis was performed in MATLAB.

3. Results

3.1. Custom wearable LSFI sensor design and operation

A small LSFI system was developed with a wearable "wristwatch" form that continuously and non-invasively monitors peripheral perfusion for early detection of hemorrhage. Software controls the laser module and camera sensor, performs real-time video capture and data processing, and transfers data via Bluetooth to external devices (Fig. 1).

3.2. Impact of camera system parameters on laser speckle

The custom double-lens Raspberry Pi camera system characteristics for two recording modes: 80 and 100 frames per second (fps), are outlined in Table 1. The focal length of the single lens system is 3.04 mm and the f/# is 2.0. As the first inverted lens acts simply as a collimator, the focal length and f/# of the fixed focus lens can be used to describe the double lens system. The aperture size is calculated to be 1.52 mm, consistent with the physical measurement of the aperture.

For images captured at the default 80 and 100 fps settings, the pixel size is 2.24 µm and 4.48 µm with 2x and 4x binning, respectively. The object distance per pixel calculated from 80 and 100 fps video captures was 2.24 and 4.47 µm, respectively. As expected, this resulted in equivalent magnifications of ~1.0x under both conditions. The calculated speckle size was 7.73 µm (Eq. (3) in Methods), which was equal for both modes. Thus, for the 80 and 100 fps imaging rates a speckle-to-pixel ratio of 3.45 and 1.72 was calculated, respectively. At 100 fps, the Nyquist criterion was not achieved, while the 80 fps sampling rate surpassed Nyquist. The two methods, from lowest to highest fps, produced different resolutions: 2.5 and 3.9 µm, respectively.

3.3. Laser characterization

The low-cost laser used in the wearable device was stable over a six-hour monitoring period and the performance of this laser was comparable to that of a highly coherent and stable benchtop

Biomedical Optics EXPRESS

Table 1. Calculated double lens system camera parameters.

Method	80 fps 640p	100 fps 320p
Focal length	3.04 mm	3.04 mm
Lens diameter	1.52 mm	1.52 mm
f/#	2.0	2.0
Camera pixel size	2.24 × 2.24 µm	4.48 × 4.48 µm
Distance per pixel	2.24 µm	4.47 µm
Magnification	1.00x	1.00x
Speckle size	7.73 µm	7.73 µm
Speckle:Pixel ratio	3.45	1.72
Spatial resolution	2.5 µm	3.9 µm

laser that served as a benchmark (Fig. 2(A)-(B)). The benchmark laser had a peak wavelength of 785.12 nm at room temperature and varied within a range of 0.607 nm. The peak wavelength of the low-cost laser was 791.25 nm at room temperature, and the variation was within a range of 0.605 nm if the temperature was held constant (fig. S1).

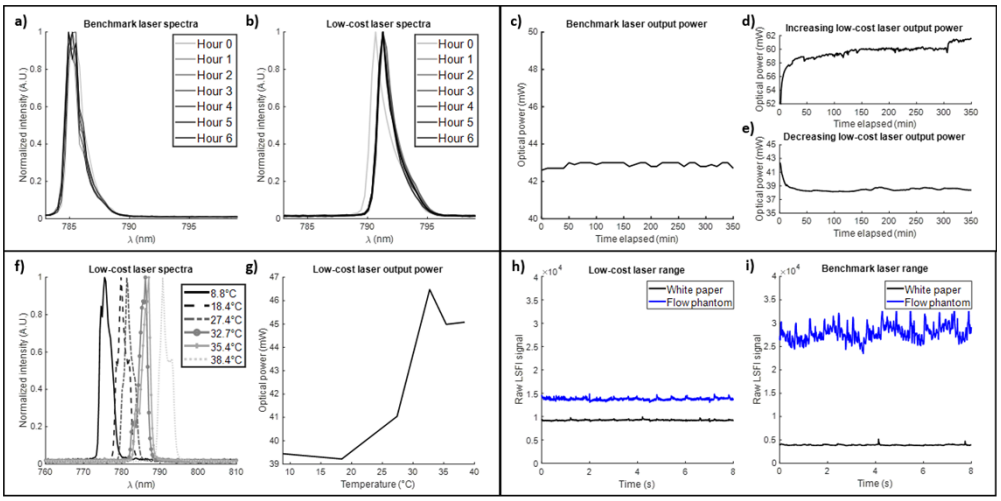

Fig. 2. Laser characterization. Overlayed spectra of the benchmark (a) and low-cost laser (b) every hour for six hours. Optical power output of the benchmark laser (c), an initially increasing low-cost laser (d), and an initially decreasing low-cost laser (e). Low-cost laser spectra (f) and optical power output (g) over temperatures ranging from 8.8-38.4°C. Range of LSFI values produced by benchmark laser (h) and low-cost laser (i) while measuring static and moving media at 5 ms exposure time.

During a six-hour period, the output optical power of the benchmark laser and multiple low-cost lasers were recorded. The benchmark laser produced an average output power of 42.90 mW and varied within a range of 0.40 mW or 0.9% (Fig. 2(C)). A batch of identical low-cost lasers from a single vendor were tested, and some decreased in the initial twenty-minute period, while others increased (Fig. 2(D)-(E)). The optical power of the low-cost laser had a percent change of 13.8% and 8.6% for the increasing and decreasing lasers, respectively, within the first twenty minutes of measurement. The lasers remained stable for the remaining period with a percent change of 6.3% and 0.9%, respectively. For the low-cost lasers, intra-laser variability was low, but inter-laser

Biomedical Optics EXPRESS

variability was high. Unique laser identifiers tracked the use of each of the characterized lasers for the subsequent experiments.

The low-cost laser does not come equipped with a temperature-regulating driver, thus, characterizing the impact of temperature on laser stability is crucial. Decreasing the temperature of the laser caused lower optical power output and a lower peak wavelength (Fig. 2(F)-(G)).

The maximum and minimum LSFI values for each laser were characterized (Fig. 2(H)-(I)) by measuring white paper and a flow phantom, respectively. Using the benchmark laser, the minimum and maximum LSFI values were 3,913 and 27,960, respectively, with a total range of 24,050. The low-cost laser system produced a minimum and maximum LSFI value of 9,241 and 13,820, respectively, with a range of 4,574. The benchmark laser produced a broader range of LSFI values and higher and lower absolute values in the static and dynamic conditions.

3.4. Device power consumption

The device consumed 0.85 W (170 mAh) during idle status and 2 W during full operation (410 mAh) (Table S1). The PiSugar battery has a maximum capacity of 1200 mAh, and thus the battery life will last approximately 3 hours when actively collecting data.

3.5. Device performance in vitro

As expected, the relationship between mean LSFI and fluid velocity was linear in the low-cost and benchtop laser systems, with a strong correlation coefficient of 1 and 0.99 achieved, respectively (Fig. 3). In addition, the benchtop laser exhibited a steeper slope (8411) compared to the low-cost laser (6514).

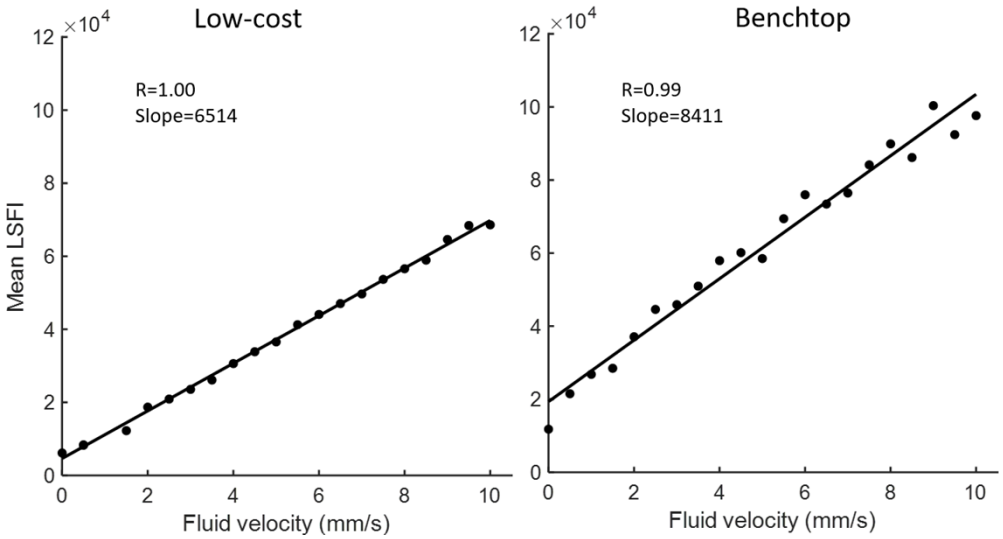

Fig. 3. Comparison of linear response to fluid velocity between low-cost and benchtop lasers. Mean LSFI measured while recording various physiological blood velocities with 0.5 ms exposure time.

3.6. Device performance in swine model of hemorrhage

Plots of the peak-normalized mean LSFI signal per minute of the study for each swine (Fig. 4) displayed the relationship of each response to hemorrhage and crystalloid resuscitation. Net fluid, represented as a percentage of EBV, is defined as the total fluids added to the swine through IV catheters minus the total fluids removed from the swine through blood loss. Because different

Biomedical Optics EXPRESS

swine received different fluid volumes through the IV catheters, the change in net fluids as a percentage of EBV varied across swine. However, when just considering the blood removed from the swine, a maximum of 40% EBV was removed from each. There was a distinct decrease in LSFI signal during periods of blood draw matching the rate of removal and an apparent increase in LSFI during subsequent crystalloid infusions in all models except swine 5. Unlike other swine, swine 5 was heparinized. Heparin has been reported to inhibit vasoconstriction, and therefore the swine's ability to vasoconstrict in response to blood loss may have been affected [41–44]. Due to this fact, swine 5 was not considered during subsequent quantitative analysis. At the start of the blood draw, swine 1-6 had been given IV fluids volumes of 740, 870, 390, 564, 438, and 168 mL, respectively, which reflect differences in the length of time it took to prepare each swine for the experiment. Swine 1 experienced vein collapse in the left femoral vein towards the end of the blood draw procedure. The vein collapse was discovered as it became challenging to draw blood from the swine and was detected as a momentary increase in LSFI signal on the laser speckle device. Additionally, swine 4 experienced a blood clot during the crystalloid infusion phase, which was identified by the veterinary staff and was also detected by the laser speckle device as a sharp decrease in the LSFI signal.

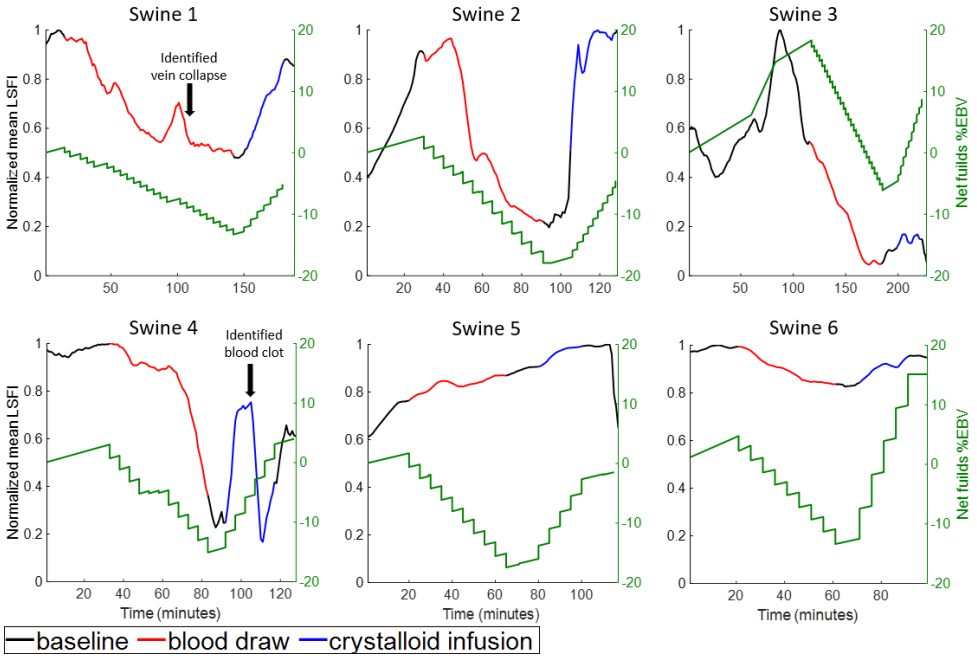

Fig. 4. Wearable LSFI response during swine hemorrhage and resuscitation. Peak-normalized mean LSFI signal captured before hemorrhage (black), during hemorrhage (red), and during crystalloid resuscitation (blue) studies compared to net fluid change (green) for each of six swine.

The baseline LSFI signal for swine 3 varied more than other swine during the alteration of isoflurane dosage (fig. S2). This deviation may have been the result of the vasoactive properties of isoflurane as each swine may have a distinct response to the drug. Swine 3 received a much higher dose of isoflurane (3%) compared to other swine (1.5-2%). Other swine also required titration of the isoflurane dose throughout the procedure to prevent manual breathing.

Overlays of HR, MAP, and SI with the peak-normalized mean LSFI signal over time revealed minimal correlation between LSFI and HR, similar responses between LSFI and MAP, and an inverse response between LSFI and SI for each swine (fig. S3-5). Swine were given oxygen

Biomedical Optics EXPRESS

throughout the procedure, resulting in highly stable SpO_2 measures (fig. S6) (range of 92-100% SpO_2). Swine 4 experienced SpO_2 values as low as 92 during severe hemorrhage and when a blood clot was identified. It is anticipated that if the swine were not given supplemental oxygen, the SpO_2 values would have been lower, particularly at severe hemorrhage stages, in all swine. Continuous vital sign recordings were not available for swine 1; instead, measurements were recorded every 15 minutes. In addition, LSFI, MAP, HR, and SI were correlated with net fluid change for each swine during hemorrhage (Fig. 5) and resuscitation (Fig. 6). LSFI was normalized by the initial signal at the start of hemorrhage and resuscitation, respectively. During hemorrhage, LSFI had the highest correlation of −0.94 (average of each swine's correlation coefficient) with a net fluid loss compared to other vital signs monitored. MAP had similar trends as LSFI with net fluid change of −0.92. HR had a correlation of 0.14, which was significantly worse than all other measures. SI had a correlation of 0.88 and an inverse trend to LSFI. Additionally, the correlation between net fluids and pooled LSFI, SI, MAP, and HR across all swine was −0.80, 0.76, −0.84, and 0.20, respectively.

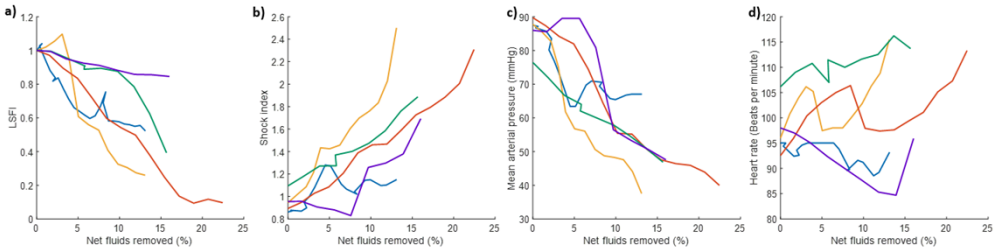

e)

		Swine 1	Swine 2	Swine 3	Swine 4	Swine 6	Average	Across all swine
LSFI	r	-0.90	-0.95	-0.99	-0.90	-0.98	**-0.94**	**-0.80**
	slope	-0.035	-0.073	-0.046	-0.033	-0.010	-0.040	-0.039
SI	r	0.61	0.96	0.99	0.98	0.85	**0.88**	**0.76**
	slope	0.018	0.10	0.058	0.049	0.045	0.053	0.052
MAP	r	-0.79	-0.95	-0.97	-0.99	-0.91	**-0.92**	**-0.84**
	slope	-1.6	-3.8	-2.4	-1.8	-3.0	-2.5	-2.2
HR	r	-0.69	0.58	0.62	0.83	-0.62	**0.15**	**0.20**
	slope	-0.37	0.74	0.46	0.50	-0.56	-0.16	0.29

Fig. 5. Response of LSFI sensor and vital signs during swine hemorrhage. Correlation between LSFI (a), shock index (SI) (b), mean arterial pressure (MAP) (c), and heart rate (HR) (d) vs net fluid change since the start of blood removal for each swine during blood loss only. (e) Summary of correlation coefficients and slopes for each case. "Average" takes the correlation coefficient from each individual swine and averages the values. "Across all swine" groups all the swine datapoints together and calculates a single correlation from the pooled data.

During resuscitation, LSFI demonstrated a strong positive correlation (average of each swine's correlation coefficient) with net fluid change (r = 0.79), whereas MAP, HR, and SI had poorer correlation with net fluid change, with correlation coefficients of −0.75, 0.16, and −0.05 respectively (Fig. 6). Data collected from swine 4 following the detected blood clot was omitted from this analysis. In addition, the correlations between net fluids into the swine and pooled LSFI, SI, MAP, and HR across swine were 0.24, −0.19, −0.04, and −0.16, respectively.

While our primary outcome measure was changes in net fluids because this is the cause of hemorrhage, we also tested the correlation between LSFI, MAP, and SI (fig. S7) as these are valid indicators of hemorrhage that can more easily be measured in clinical conditions, particularly SI. LSFI vs. MAP showed a strong correlation during hemorrhage (r = 0.93), but a weak correlation

Biomedical Optics EXPRESS

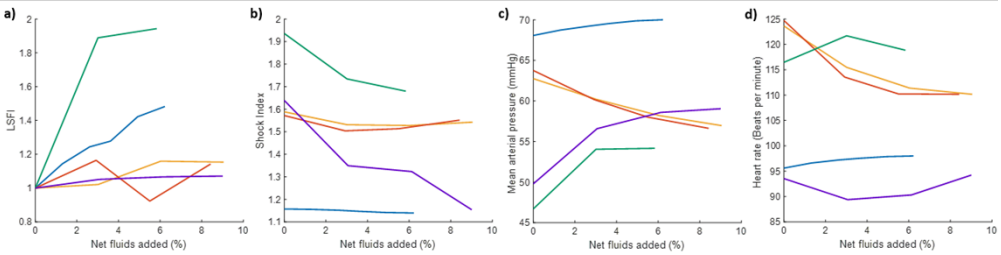

e)

		Swine 1	Swine 2	Swine 3	Swine 4	Swine 6	Average	Across all swine
LSFI	r	0.991429	0.913118	0.231765	0.898687	0.909913	**0.7890**	**0.2386**
	slope	0.076511	0.019852	0.007436	0.163011	0.007619	1.2178	0.0219
SI	r	-0.98673	-0.64906	-0.21199	-0.95485	-0.95048	**-0.7506**	**-0.1928**
	slope	-0.00316	-0.00467	-0.00188	-0.04408	-0.04923	-1.1585	-0.0151
MAP	r	0.976554	-0.98901	-0.97871	0.881988	0.903551	**0.1589**	**-0.0434**
	slope	0.311525	-0.64218	-0.84506	1.290158	0.994113	4.2970	-0.0975
HR	r	0.955213	-0.94407	-0.8829	0.471446	0.150476	**-0.0500**	**-0.1557**
	slope	0.375608	-1.47366	-1.68736	0.4229	0.092136	-2.2877	-0.5980

Fig. 6. Response of LSFI sensor and vital signs during swine resuscitation. Correlation between LSFI (a), shock index (SI)(b), mean arterial pressure (MAP) (c), and heart rate (HR) (d) vs. net fluid change in each swine since the start of crystalloid infusion. (e) Summary of correlation coefficients and slopes from linear fitting for each case. "Average" takes the correlation coefficient from each individual swine and averages the values. "Across all swine" groups all the swine datapoints together and calculates a single correlation from the pooled data.

during resuscitation ($r = 0.36$). Similar findings were observed when performing a correlation of LSFI vs. SI during hemorrhage ($r = -0.90$) and resuscitation ($r = -0.79$).

3.7. Laser speckle video parameter analysis

The raw, unsmoothed LSFI signal produced throughout the hemorrhage procedure was down-sampled by frame rate from 100 fps to 50 and 10 fps. In addition, the frame size was varied from a full frame to one half- and one quarter-frames. The down-sampled frame rate and frame size of the entire swine hemorrhage study resulted in minimal changes in the mean LSFI trend result and the net fluid input vs. LSFI correlation coefficient (fig. S8).

4. Discussion

Hemorrhage can be a devastating complication of not only childbirth, but also trauma, surgery, and bleeding disorders. Tools that can provide an early indication of concerning blood loss could transform management from reactive to preventive, particularly in the postpartum setting. Herein, we present a low-cost, light-based sensor worn on the periphery to monitor for early compensatory mechanisms triggered by blood loss, which was validated in a swine model of hemorrhage and resuscitation. The literature has long described peripheral vasoconstriction as one of the earliest physiologic compensatory mechanisms to protect vital organs from hypo-perfusion and overall cardiovascular collapse [22,23]. However, this compensation also blunts vital sign responses in the setting of ongoing blood loss, preventing early diagnosis. We demonstrated the feasibility of this approach in swine studies, during which we observed significant and near-immediate decreases and increases in LSFI signal during hemorrhage and resuscitation, respectively.

All swine except for the heparinized swine 5 experienced an overall decrease in LSFI during blood loss, indicative of peripheral vasoconstriction in response to hypovolemia. Heparin has been shown to cause vasodilation and lower blood pressure [45,46], particularly when administered

Biomedical Optics EXPRESS

as a bolus, as it was administered in swine 5. Further, heparin has been shown to reduce the endothelial release of the vasoconstrictor endothelin-1 [47] as well as reduce blood viscosity, both of which can affect perfusion. Thus, swine 5 was excluded from quantitative analysis. The quantitative analysis of the correlation between blood loss and LSFI in swine revealed a striking average correlation coefficient of −0.94. The correlation coefficient of LSFI and blood loss across swine was −0.80, which is similar to the correlation coefficient of blood loss and MAP ($r = -0.84$) and greater than the correlation coefficients of blood loss with SI and HR. In future studies, individual calibration will be performed by normalizing the LSFI signal using the minimum blood flow state of a subject produced during occlusion to allow for more accurate inter-subject LSFI comparison. Unlike the other non-heparinized swine, swine 2 exhibited an increase in LSFI at the beginning of the hemorrhage procedure followed by a rapid decline. We do expect some biological variability across swine, but also note that swine 2 had the largest amount of IV fluids given prior to the start of the hemorrhage procedure began. It is possible that in this swine, more blood loss was required to initiate a compensatory response. During resuscitation, all non-heparinized swine showed a net increase in LSFI signal, however, swine 3 exhibited a much milder increase than the others. This swine had the greatest volume of blood removed, and the LSFI signal reached a plateau at the last seven blood withdrawals of the hemorrhage phase. This swine likely experienced hypovolemia to the extent of cardiovascular collapse, and the resuscitation fluids provided were not sufficient to re-start cardiovascular flow. A milder response in this case should not be considered a limitation of the technique, but rather, it reflects the true cardiovascular state in response to resuscitation.

In addition to measuring LSFI as a function of net fluid change, we also compared the response of vital signs and SI throughout the hemorrhage and resuscitation procedure. MAP and SI correlated well with blood loss and resuscitation, but LSFI had superior performance in both settings, which supports the utility of using LSFI for hemorrhage detection and management. In these swine studies conducted under general anesthesia, vital signs, particularly MAP, deteriorated quickly with hemorrhage, which does not mimic the common clinical manifestation in which MAP and/or blood pressure is maintained until moderate to severe blood loss. MAP is calculated by multiplying CO and SVR. General anesthesia acts as a vasodilator, and thus compensatory responses were likely blunted, reducing the magnitude of vasoconstriction and consequently SVR, compared to the scenario of maintained blood pressure. In particular, isoflurane has been shown to inhibit sympathetic response to hypovolemia [48–51]. In future patient studies, we anticipate observing a delay in vital sign deterioration in accordance with the literature [13,14,22,23], as the vast majority of delivering patients are not under general anesthesia.

Some variability across different patients' degrees of sympathetic nervous system response to hemorrhage is expected. Patients with cardiovascular disease may have dampened ability to vasoconstrict due to vessel stiffening. Pharmacologic agents may also dampen the vasoconstriction response (such as the effects of anesthesia in this study which likely contributed to blood pressures dropping with blood loss). In the scenario that LSFI decreases at a similar rate to MAP, as observed in these swine studies, it is important to emphasize that an arterial line connected to a SurgiVet Monitor obtained the MAP and recorded data every 6 seconds. In pregnancy, placement of arterial lines is rare due to the high potential for complications; thus, > 99% of patients do not have invasive arterial lines. Instead, blood pressure is typically measured using a pneumatic cuff following the oscillometric method, which requires more than 1 minute for a single reading. Our device can currently record at a frequency of 100 Hz and perform frame-by-frame processing at 80 Hz. Swine data was recorded for 10 seconds once per minute, then processed and transmitted to a receiving device with a 15-20 second delay, allowing for near real-time data visualization and examination of LSFI trends. However, we anticipate real-time capabilities (≥30 Hz data processing + transmission) in future iterations. Therefore, our wearable LSFI system would still provide an earlier indication of hemorrhage risk than blood pressure (BP) due to its rapid

Biomedical Optics EXPRESS

sampling and data transmission capabilities. In the setting of PPH, a delay in diagnosis of 1-2 minutes can be the difference between life and death. In addition to low sampling rates for BP, studies have demonstrated that oscillometric-based BP cuffs, such as those used in laboring and cesarean delivery patients in hospital settings, perform poorly in hypotensive situations, providing falsely high values that could mask hemorrhage [52].

It is also crucial to note that LSFI and BP are not measuring the same phenomenon. While the measures are related, they provide distinct information. While LSFI did correlate strongly with BP during hemorrhage, this was not maintained during resuscitation (correlation between LSFI and MAP of 0.36, fig S7), demonstrating that mean LSFI is not a direct measure of BP and is instead a measure of peripheral vascular resistance. There are many situations that would benefit from having both pieces of information. For instance, medical decisions would likely differ based on different combinations of MAP and LSFI values. In the case of low MAP and low LSFI (low peripheral perfusion), providers would likely interpret this situation as dangerously low blood volume that needs immediate treatment with either fluids or transfusion. However, in the case of low MAP and normal LSFI, they may instead opt to administer a peripheral vasoconstriction medication to help the patient compensate for mild blood loss and as a result, increase BP, without the need for blood transfusion.

While characterizing our wearable's performance, we found that, as expected, pairing our low-cost laser with the LSFI wearable device exhibited reduced sensitivity to changes in velocity than the highly coherent benchtop laser and less power stability across a range of ambient temperatures. However, the size and cost of the benchtop laser are prohibitive in being used for wearable applications and the sensitivity to velocity changes was within 75% of the benchmark laser, demonstrating sufficient resolution for the expected in vivo range of velocities. Our wearable system effectively produced a linear response to changes in flow rate, similar to reported findings using high-cost systems [27], and successfully detected peripheral perfusion changes in a swine model of hemorrhage and resuscitation, the main criteria for this application. The low-cost laser diode is roughly $12 \times 12 \times 8$ mm (width x height x depth) in size, while the benchtop laser, which consists of two separate constant current and temperature drivers that together weigh over 6 kg, require approximately $146 \times 154 \times 320$ mm of space.

The Raspberry Pi camera system allowed for speckle-to-pixel ratios that surpassed the Nyquist rate when using the 640p at 80 fps mode. Swine data was collected while recording at 320p and 100 fps which did not meet the Nyquist sampling criterion, although it approached it. Even without meeting this criterion, the swine data produced promising results, which will improve when the frame rate and consequently pixel binning are reduced. Fig. S8 demonstrates that decreasing the frame rate will not deleteriously affect the conclusions drawn from the data or the data quality. With the Raspberry Pi camera, decreasing the frame rate is a simple way to increase speckle size, reduce computation load and needed speed, and improve image quality. A second mechanism to increase the speckle size and the speckle-to-pixel ratio is to decrease the aperture of the camera system, however, this will reduce the amount of light detected by the camera. In addition, reducing the image window size may provide an alternate means to maintain high frame rates (>80 fps) without binning.

Our wearable LSFI sensor is part of a growing group of technologies that measure the physiological response to hemorrhage by interrogating the vasculature. Optical spectroscopy-based sensors tracking longitudinal hemoglobin (Hb) concentration changes caused by postpartum blood loss [53–58] reported larger bias and decreased accuracy between gold standard Hb measurements compared to similar studies conducted in non-pregnant subjects [53,54,56]. Some authors stated that the devices may need pregnancy-specific calibration prior to successful use in obstetric care. A recent study successfully employed machine learning to improve Hb concentration performance in pregnant patients [59], thus, demonstrating that this approach could be further improved for use in pregnancy. One drawback of Hb concentration approaches is that

Biomedical Optics EXPRESS

the rate of interstitial fluid transfer to the vasculature is unknown and significant decreases in Hb concentration may take tens of minutes to hours, limiting the utility of this approach in detecting rapid PPH. However, Hb concentration is a principal guide during massive hemorrhage and PPH resuscitation efforts and therefore is still of clinical value in PPH care.

Researchers have also mined photoplethysmography (PPG) waveforms, the signals acquired from pulse oximeters, to develop predictive algorithms for hemorrhage in military, trauma, and critical care settings [60]. While these algorithms show promise, PPG has multiple draw backs, including low SNR, particularly in patients with poor perfusion [61,62], as expected during hemorrhage. Furthermore, PPG-based measurements on patients with darkly pigmented skin have lower SNR, which can lead to errors when extracting cardiovascular features from PPG waveforms and could contribute to additional racial disparities in maternal health [63,64].

More recently, investigators have begun targeting the peripheral vasoconstriction compensation mechanism as an early indicator of dangerous blood loss. One study evaluated peripheral perfusion using the perfusion index, a pulse oximeter parameter that tracks perfusion based on the ratio of the pulsatile to non-pulsatile signal, to track postpartum blood loss in patients who underwent vaginal delivery. A correlation of −0.7 was found between blood loss and the difference in perfusion index immediately and 20 minutes postpartum [65]. Although the perfusion index is known to be skewed and has high patient variability [66], these results show that non-invasive measures of peripheral vasoconstriction can provide early signs of postpartum blood loss. An alternate strategy to the perfusion index is using dynamic light scattering (DLS) to monitor blood flow. A miniaturized DLS (mDLS) system was developed [67] and tested in a swine hemorrhage model, where mDLS signals changed in a proportionate manner to blood loss. A recent review article provided preliminary results from a thermal dissipation sensor, which observed a correlation with postpartum blood loss ($r = 0.22$) [68].

Our wearable LSFI sensor has numerous advantages over the aforementioned methods. LSFI has demonstrated significantly higher SNR than PPG [29,69] which measures changes caused by light scattering rather than PPG measurements of absorption. Furthermore, tests quantifying the effects of skin pigmentation in both phantom measurements and patient studies found no significant difference based on the level of pigmentation [31]. LSFI has a broad dynamic range with linear response to blood flow even in low perfusion conditions [29], which overcomes limitations of the PPG-derived perfusion index. While LSFI and mDLS share similarities in what is being measured, by using a camera consisting of thousands of photodetectors instead of a single photodetector, LSFI provides a higher SNR with relatively simple and low-cost instrumentation. In contrast to thermal dissipation sensors which measure a surrogate of perfusion, LSFI directly measures changes in perfusion, and has been shown to be highly sensitive to small changes in perfusion [27], providing high contrast between states of vasoconstriction and vasodilation.

Current limitations of the device include the fact that the device measures relative values of blood velocity/flow rather than absolute measurements. This is a limitation that affects all laser speckle-based imaging devices and is an active area of research within the laser speckle imaging community. Some advancements have been made on this front, in which using a wide range of exposure times allows for a more accurate estimation of blood velocity [70]. An alternate method to aid data interpretation includes taking an occlusion baseline, during which a pneumatic cuff is inflated to restrict blood flow, and normalizing data by this "zero blood flow" value as an estimate of a patient's absolute minimum LSFI value. In addition, the current device is relatively bulky and has high power consumption, which will both need to be reduced in future iterations to achieve an ergonomic footprint and battery life. Over 90% of PPHs occur within 24 hours postpartum, thus an ideal battery would last >24 hours. Additional features should allow for optimization of the device parameters for each experiment, helping to ensure high SNR and large velocity dynamic range. Such features include autofocus and adjustable light intensity via altering exposure time or varying laser power until a desired light level is reached and then set for the

Biomedical Optics EXPRESS

duration of the experiment. The largest limitation of the current device is laser instability, which can be corrected by developing more sophisticated laser driver circuitry and testing new compact and inexpensive laser diode options. Limitations of this study include the omission of potential sources of speckle noise, such as read, shot, and quantization noise [71,72], which should be factored into the LSFI processing pipeline of future studies. In addition, our hemorrhage model did not fully recapitulate the expected hemodynamics of maintained BP at early- to mid-stages of hemorrhage, as MAP also decreased with decreasing blood loss. Future animal studies will improve the model to reflect the maintenance of MAP observed clinically. A final set of limitations that pertain to peripheral perfusion monitoring systems include the possibility of false positive results due to peripheral vasoconstriction that is not associated with blood loss. This can be caused by vasoactive medications (such as phenylephrine or epinephrine), and it will be important for the healthcare personnel using these devices to track any pharmaceuticals given during use. Importantly, such medications will impact all vital signs, and it is standard for medical teams to monitor and interpret the hemodynamic effects of pharmacologic agents. Adding peripheral perfusion information will provide a more holistic view of the cardiovascular response to such medications.

5. Conclusion

In summary, we have demonstrated that a custom wearable laser speckle imaging device could rapidly detect hemorrhage-driven peripheral vasoconstriction and resuscitation via crystalloid infusion. This progress provides a framework for a novel low-cost and noninvasive technology that identifies ongoing blood loss when low-cost and accessible interventions are effective, with the hope of reducing the unacceptably high rates of maternal morbidity and mortality caused by hemorrhage in low- and high-resource settings alike.

Funding. Eunice Kennedy Shriver National Institute of Child Health and Human Development (K99HD103954, R00HD103954); Washington University in St. Louis (Women's Health Technologies Collaboration Init.).

Acknowledgments. The authors gratefully acknowledge helpful discussions and feedback from Joe Culver, Chen-Hao (Paul) Lin, Ed Richter, Sam Achilefu, Sarah England, David Monks, Patricia Strutz, Mike Dombrowski, Roxane Rampersad, Deborah Frank, Molly Stout, and Kathleen Duncan.

Disclosures. Armor Medical (CO, LS), PCT/US2022/021048, "Hemodilution detector" (FBM, CO, LS)

Data availability. All data, code, and materials used in the analysis are available for non-commercial research purposes upon reasonable request and may include a material/data transfer agreement.

Supplemental document. See Supplement 1 for supporting content.

References

1. L. Say, D. Chou, A. Gemmill, Ö. Tunçalp, A.-B. Moller, J. Daniels, A. M. Gülmezoglu, M. Temmerman, and L. Alkema, "Global causes of maternal death: a WHO systematic analysis," The Lancet global health **2**(6), e323–e333 (2014).
2. B. Lawton, E. J. MacDonald, S. A. Brown, L. Wilson, J. Stanley, J. D. Tait, R. A. Dinsdale, C. L. Coles, and S. E. Geller, "Preventability of severe acute maternal morbidity," Am. J. Obstet Gynecol. **210**(6), 557.e1–557.e6 (2014).
3. J. J. Zwart, J. M. Richters, F. Ory, J. I. de Vries, K. W. Bloemenkamp, and J. van Roosmalen, "Severe maternal morbidity during pregnancy, delivery and puerperium in the Netherlands: a nationwide population-based study of 371,000 pregnancies," BJOG : An International J. Obstetrics and Gynaecol. **115**(7), 842–850 (2008).
4. S. E. Geller, D. Rosenberg, S. M. Cox, M. L. Brown, L. Simonson, C. A. Driscoll, and S. J. Kilpatrick, "The continuum of maternal morbidity and mortality: Factors associated with severity," Am. J. Obstet. Gynecol. **191**(3), 939–944 (2004).
5. C. J. Berg, M. A. Harper, S. M. Atkinson, E. A. Bell, H. L. Brown, M. L. Hage, A. G. Mitra, K. J. Moise Jr., and W. M. Callaghan, "Preventability of pregnancy-related deaths: results of a state-wide review," Obstet Gynecol. **106**(6), 1228–1234 (2005).
6. E. A. Howell, "Reducing Disparities in Severe Maternal Morbidity and Mortality," Clin. Obstet. Gynecol. **61**(2), 387–399 (2018).
7. "Building U. S. Capacity to Review and Prevent Maternal Deaths, "Report from nine maternal mortality review committees"," (Atlanta, GA, 2018).

Biomedical Optics EXPRESS

8. C. Deneux-Tharaux, M. Bonnet, and J. Tort, "Epidemiology of post-partum haemorrhage," J. Gynecol. Obstet. Biol. Reprod. (Paris) **43**(10), 936–950 (2014).
9. Y. Wang, "Vascular biology of the placenta," in *Colloquium Series on Integrated Systems Physiology: From Molecule to Function*, (Morgan & Claypool Life Sciences, 2010), 1–98.
10. M. E. D'Alton, K. M. Rood, M. C. Smid, H. N. Simhan, D. W. Skupski, A. Subramaniam, K. S. Gibson, T. Rosen, S. M. Clark, and D. Dudley, "Intrauterine vacuum-induced hemorrhage-control device for rapid treatment of postpartum hemorrhage," Obstet. Gynecol. **136**(5), 882–891 (2020).
11. J. M. Anderson and D. Etches, "Prevention and management of postpartum hemorrhage," Am. Fam. Physician **75**(6), 875–882 (2007).
12. S. Miller, F. Lester, and P. Hensleigh, "Prevention and treatment of postpartum hemorrhage: new advances for low-resource settings," J. Midwifery Womens Health **49**(4), 283–292 (2004).
13. J. C. Schadt, "Sympathetic and hemodynamic adjustments to hemorrhage: A possible role for endogenous opioid peptides," Resuscitation **18**(2-3), 219–228 (1989).
14. L. Xiang, C. Hinojosa-Laborde, K. L. Ryan, C. A. Rickards, and V. A. Convertino, "Time course of compensatory physiological responses to central hypovolemia in high- and low-tolerant human subjects," Am. J. Physiol. Regul. Integr. Comp. Physiol. **315**(2), R408–R416 (2018).
15. "Practice Bulletin No. 183: Postpartum Hemorrhage," Obstetrics & Gynecology **130** (2017).
16. M. Natrella, E. Di Naro, M. Loverro, N. Benshalom-Tirosh, G. Trojano, D. Tirosh, L. Besser, M. T. Loverro, and S. A. Mastrolia, "The more you lose the more you miss: accuracy of postpartum blood loss visual estimation. A systematic review of the literature," The J. Maternal-Fetal & Neonatal Medicine **31**(1), 106–115 (2018).
17. A. Hancock, A. D. Weeks, and D. T. Lavender, "Is accurate and reliable blood loss estimation the 'crucial step' in early detection of postpartum haemorrhage: an integrative review of the literature," BMC Pregnancy Childbirth **15**(1), 230 (2015).
18. C. E. Majors, C. A. Smith, M. E. Natoli, K. A. Kundrod, and R. Richards-Kortum, "Point-of-care diagnostics to improve maternal and neonatal health in low-resource settings," Lab Chip **17**(20), 3351–3387 (2017).
19. A. F. Rubenstein, M. Block, S. Zamudio, C. Douglas, S. Sledge, G. Tully, and R. L. Thurer, "Accurate assessment of blood loss during cesarean delivery improves estimation of postoperative hemoglobin," Amer. J. Perinatol. **36**(4), 434–439 (2019).
20. H. L. Nathan, A. El Ayadi, N. L. Hezelgrave, P. Seed, E. Butrick, S. Miller, A. Briley, S. Bewley, and A. H. Shennan, "Shock index: an effective predictor of outcome in postpartum haemorrhage?" BJOG: Int. J. Obstet. Gy. **122**(2), 268–275 (2015).
21. S.-Y. Lee, H.-Y. Kim, G.-J. Cho, S.-C. Hong, M.-J. Oh, and H.-J. Kim, "Use of the shock index to predict maternal outcomes in women referred for postpartum hemorrhage," Intl. J. Gynecology & Obste. **144**(2), 221–224 (2019).
22. W. R. Cohen, "Hemorrhagic shock in obstetrics," J. Perinat. Med. **34**(4), 263–271 (2006).
23. V. A. Convertino, N. J. Koons, and M. R. Suresh, "Physiology of Human Hemorrhage and Compensation," in *Comprehensive Physiology* (2021), pp. 1531–1574.
24. K. L. Ryan, C. A. Rickards, C. Hinojosa-Laborde, W. H. Cooke, and V. A. Convertino, "Sympathetic responses to central hypovolemia: new insights from microneurographic recordings," Front. Physio. **3**, 110 (2012).
25. A. R. Pries and T. W. Secomb, "Chapter 1 - Blood Flow in Microvascular Networks," in *Microcirculation (Second Edition)*, R. F. Tuma, W. N. Durán, and K. Ley, eds. (Academic Press, 2008), pp. 3–36.
26. B. Lertsakdadet, C. Dunn, A. Bahani, C. Crouzet, and B. Choi, "Handheld motion stabilized laser speckle imaging," Biomed. Opt. Express **10**(10), 5149–5158 (2019).
27. B. Choi, J. Ramírez-San-Juan, J. Lotfi, and J. Nelson, "Linear response range characterization and in vivo application of laser speckle imaging of blood flow dynamics," J. Biomed. Opt. **11**(4), 041129 (2006).
28. D. A. Boas and A. K. Dunn, "Laser speckle contrast imaging in biomedical optics," J. Biomed. Opt. **15**(1), 011109 (2010).
29. M. Ghijsen, T. B. Rice, B. Yang, S. M. White, and B. J. Tromberg, "Wearable speckle plethysmography (SPG) for characterizing microvascular flow and resistance," Biomed. Opt. Express **9**(8), 3937–3952 (2018).
30. C. Huang, M. Seong, J. P. Morgan, S. Mazdeyasna, J. G. Kim, J. T. Hastings, and G. Yu, "Low-cost compact diffuse speckle contrast flowmeter using small laser diode and bare charge-coupled-device," J. Biomed. Opt. **21**(8), 080501 (2016).
31. T. B. Rice, B. Yang, and S. White, "Effect of skin optical absorption on speckleplethysmographic (SPG) signals," Biomed. Opt. Express **11**(9), 5352–5361 (2020).
32. A. Fülöp, Z. Turóczi, D. Garbaisz, L. Harsányi, and A. Szijártó, "Experimental models of hemorrhagic shock: a review," Eur. Surg. Res. **50**(2), 57–70 (2013).
33. A. N. S. Institute, "Z136.1 American National Standard for Safe Use of Lasers," Laser Institute of America, Orlando, FL (2014).
34. G. Zonios, A. Dimou, I. Bassukas, D. Galaris, A. Tsolakidis, and E. Kaxiras, "Melanin absorption spectroscopy: new method for noninvasive skin investigation and melanoma detection," J. Biomed. Opt. **13**(1), 014017 (2008).
35. A. P. Mary, E. R. Robert, J. C. V. George, J. G. Maxwell, H. Ryan, L. Edward, and F. P. James, "Laying the foundation to use Raspberry Pi 3 V2 camera module imagery for scientific and engineering purposes," J. Electron. Imaging **26**(1), 013014 (2017).

Biomedical Optics EXPRESS

36. N. A. Switz, M. V. D'Ambrosio, and D. A. Fletcher, "Low-cost mobile phone microscopy with a reversed mobile phone camera lens," PLoS One **9**(5), e95330 (2014).
37. W. J. Tom, A. Ponticorvo, and A. K. Dunn, "Efficient processing of laser speckle contrast images," IEEE Trans. Med. Imaging **27**(12), 1728–1738 (2008).
38. F. Ye, S. Yin, M. Li, Y. Li, and J. Zhong, "In-vivo full-field measurement of microcirculatory blood flow velocity based on intelligent object identification," J. Biomed. Opt. **25**(01), 1–11 (2020).
39. M. Klarhöfer, B. Csapo, C. Balassy, J. C. Szeles, and E. Moser, "High-resolution blood flow velocity measurements in the human finger," Magn. Reson. Med. **45**(4), 716–719 (2001).
40. S. Yuan, A. Devor, D. A. Boas, and A. K. Dunn, "Determination of optimal exposure time for imaging of blood flow changes with laser speckle contrast imaging," Appl. Opt. **44**(10), 1823–1830 (2005).
41. M. L. Miranda, L. F. M. Prota, M. J. B. Silva, F. L. Sicuro, E. S. Furtado, A. O. M. Santos, and E. Bouskela, "Protective microcirculatory and anti-inflammatory effects of heparin on endotoxemic hamsters," Med. Express **1**(3), 127–134 (2014).
42. T. Kuga, Y. Ohara, H. Hata, Y. Hirakawa, A. Takeshita, and H. Tomoike, "Inhibitory effects of heparin, aspirin and ketanserin on coronary artery vasoconstriction after arterial balloon injury in hypercholesterolemic miniature pigs," J. Am. Coll. Cardiol. **22**(1), 291–295 (1993).
43. H. Xie-Zukauskas, J. Das, B. L. Short, J. S. Gutkind, and P. E. Ray, "Heparin inhibits angiotensin II-induced vasoconstriction on isolated mouse mesenteric resistance arteries through Rho-A-and PKA-dependent pathways," Vascular Pharmacol. **58**(4), 313–318 (2013).
44. L. Buzun, T. Kleszczewski, A. Kostrzewska, P. Lisowski, P. Oleksza, R. Jackowski, A. Pedzińska, and T. Hirnle, "Influence of low molecular weight heparin preparations on human internal thoracic artery contraction," Eur. J. Cardiothorac. Surg. **26**(5), 951–955 (2004).
45. A. K. Mandal, T. W. Lyden, and M. G. Saklayen, "Heparin lowers blood pressure: Biological and clinical perspectives," Kidney Int. **47**(4), 1017–1022 (1995).
46. O. Tangphao, S. Chalon, H. J. Moreno Jr, A. K. Abiose, T. F. Blaschke, and B. B. Hoffman, "Heparin-induced vasodilation in human hand veins," Clin. Pharmacol. Ther. **66**(3), 232–238 (1999).
47. M. Yanagisawa, H. Kurihara, S. Kimura, Y. Tomobe, M. Kobayashi, Y. Mitsui, Y. Yazaki, K. Goto, and T. Masaki, "A novel potent vasoconstrictor peptide produced by vascular endothelial cells," Nature **332**(6163), 411–415 (1988).
48. J. Seagard, F. Hopp, Z. Bosnjak, J. Osborn, and J. Kampine, "Sympathetic efferent nerve activity in conscious and isoflurane-anesthetized dogs," Anesthesiology **61**(3), 266–270 (1984).
49. P. Pawson and S. Forsyth, "Chapter 5 - Anesthetic agents," in *Small Animal Clinical Pharmacology (Second Edition)*, J. E. Maddison, S. W. Page, and D. B. Church, eds. (W. B. Saunders, Edinburgh, 2008), pp. 83–112.
50. C. Constantinides, R. Mean, and B. J. Janssen, "Effects of isoflurane anesthesia on the cardiovascular function of the C57BL/6 mouse," Ilar J. **52**(3), e21–e31 (2011).
51. M. S. Englehart, C. E. Allison, B. H. Tieu, L. N. Kiraly, S. A. Underwood, P. J. Muller, J. A. Differding, R. S. Sawai, A. Karahan, and M. A. Schreiber, "Ketamine-Based Total Intravenous Anesthesia Versus Isoflurane Anesthesia in a Swine Model of Hemorrhagic Shock," J. Trauma Acute Care Surg. **65**(4), 901–909 (2008).
52. A. S. Meidert, M. E. Dolch, K. Mühlbauer, B. Zwissler, M. Klein, J. Briegel, and S. Czerner, "Oscillometric versus invasive blood pressure measurement in patients with shock: a prospective observational study in the emergency department," J. Clin. Monit. Comput. **35**(2), 387–393 (2021).
53. A. Butwick, G. Hilton, and B. Carvalho, "Non-invasive haemoglobin measurement in patients undergoing elective Caesarean section," Br. J. Anaesth. **108**(2), 271–277 (2012).
54. V. Skelton, N. Wijayasinghe, S. Sharafudeen, A. Sange, N. Parry, and C. Junghans, "Evaluation of point-of-care haemoglobin measuring devices: a comparison of Radical-7™ pulse co-oximetry, HemoCue® and laboratory haemoglobin measurements in obstetric patients," Anaesthesia **68**(1), 40–45 (2013).
55. E. Hadar, O. Raban, T. Bouganim, K. Tenenbaum-Gavish, and M. Hod, "Precision and accuracy of noninvasive hemoglobin measurements during pregnancy," J. Maternal-Fetal & Neonatal Medicine **25**(12), 2503–2506 (2012).
56. A. Yoshida, K. Saito, K. Ishii, I. Azuma, H. Sasa, and K. Furuya, "Assessment of noninvasive, percutaneous hemoglobin measurement in pregnant and early postpartum women," Medical Devices (Auckland, NZ) **7**, 11–16 (2014).
57. A. S. Ahankari, A. W. Fogarty, L. J. Tata, J. Dixit, and P. R. Myles, "Assessment of a non-invasive haemoglobin sensor NBM 200 among pregnant women in rural India," BMJ Innovations **2**(2), 70–77 (2016).
58. H. Kim, S.-H. Do, J.-W. Hwang, and H.-S. Na, "Intraoperative continuous noninvasive hemoglobin monitoring in patients with placenta previa undergoing cesarean section: a prospective observational study," APM **14**(4), 423–428 (2019).
59. S. Acharya, D. Swaminathan, S. Das, K. Kansara, S. Chakraborty, D. K. R, T. Francis, and K. R. Aatre, "Non-Invasive Estimation of Hemoglobin Using a Multi-Model Stacking Regressor," IEEE J. Biomedical Health Informatics **24**(6), 1717–1726 (2020).
60. V. A. Convertino and N. J. Koons, "The compensatory reserve: potential for accurate individualized goal-directed whole blood resuscitation," Transfusion (Paris) **60**, S150–S157 (2020).
61. M. Khan, C. G. Pretty, A. C. Amies, R. Elliott, Y. S. Chiew, G. M. Shaw, and J. G. Chase, "Analysing the effects of cold, normal, and warm digits on transmittance pulse oximetry," Biomedical Sig. Process. Control **26**, 34–41 (2016).

Biomedical Optics EXPRESS

62. R. Garner, R. Kumari, P. Lanyon, M. Doherty, and W. Zhang, "Prevalence, risk factors and associations of primary Raynaud's phenomenon: systematic review and meta-analysis of observational studies," BMJ open **5**(3), e006389 (2015).
63. J. Fine, K. L. Branan, A. J. Rodriguez, T. Boonya-ananta, Ajmal, J. C. Ramella-Roman, M. J. McShane, and G. L. Coté, "Sources of Inaccuracy in Photoplethysmography for Continuous Cardiovascular Monitoring," Biosensors **11**(4), 126 (2021).
64. B. A. Fallow, T. Tarumi, and H. Tanaka, "Influence of skin type and wavelength on light wave reflectance," J. Clin. Monit. Comput. **27**(3), 313–317 (2013).
65. H. Tanaka, S. Katsuragi, K. Tanaka, T. Kawamura, M. Nii, M. Kubo, K. Osato, Y. Sasaki, and T. Ikeda, "Application of the perfusion index in obstetric bleeding," J. Maternal-Fetal & Neonatal Medicine **29**(23), 3812–3814 (2016).
66. A. Hasanin, A. Mukhtar, and H. Nassar, "Perfusion indices revisited," J. Intensive Care **5**(1), 24 (2017).
67. I. Fine, A. Kaminsky, B. Kuznik, and L. Shenkman, "A non-invasive method for the assessment of hemostasis in vivo by using dynamic light scattering," Laser Phys. **22**(2), 469–475 (2012).
68. M. G. Lord, J. A. Calderon, L. D. Pacheco, and H. K. Ahmadzia, "Emerging Technology for Early Detection and Management of Postpartum Hemorrhage to Prevent Morbidity," Am. J. Obstetrics & Gynecology MFM **5**(2), 100742 (2023).
69. C. E. Dunn, D. C. Monroe, C. Crouzet, J. W. Hicks, and B. Choi, "Speckleplethysmographic (SPG) Estimation of Heart Rate Variability During an Orthostatic Challenge," Sci. Rep. **9**(1), 14079 (2019).
70. P. S. Sivakumar, K. Kagawa, C. Crouzet, B. Choi, K. Yasutomi, and S. Kawahito, "Multi-exposure laser speckle contrast imaging using a video-rate multi-tap charge modulation image sensor," Opt. Express **27**(18), 26175–26191 (2019).
71. S. Zilpelwar, E. J. Sie, D. Postnov, A. I. Chen, B. Zimmermann, F. Marsili, D. A. Boas, and X. Cheng, "Model of dynamic speckle evolution for evaluating laser speckle contrast measurements of tissue dynamics," Biomed. Opt. Express **13**(12), 6533–6549 (2022).
72. A. Garrett, B. Kim, E. J. Sie, N. Z. Gurel, F. Marsili, D. A. Boas, and D. Roblyer, "Simultaneous photoplethysmography and blood flow measurements towards the estimation of blood pressure using speckle contrast optical spectroscopy," Biomed. Opt. Express **14**(4), 1594–1607 (2023).